

Subspace Decomposition based DNN algorithm for elliptic type multi-scale PDEs

Xi-An Li^a, Zhi-Qin John Xu^{a,b,c}, Lei Zhang^{a,b,c,*}

^a*School of Mathematical Sciences, Shanghai Jiao Tong University, Shanghai 200240, China*

^b*Institute of Natural Sciences, Shanghai Jiao Tong University, Shanghai 200240, China*

^c*MOE-LSC, Shanghai Jiao Tong University, Shanghai 200240, China*

Abstract

While deep learning algorithms demonstrate a great potential in scientific computing, its application to multi-scale problems remains to be a big challenge. This is manifested by the “frequency principle” that neural networks tend to learn low frequency components first. Novel architectures such as multi-scale deep neural network (MscaleDNN) were proposed to alleviate this problem to some extent. In this paper, we construct a subspace decomposition based DNN (dubbed SD²NN) architecture for a class of multi-scale problems by combining traditional numerical analysis ideas and MscaleDNN algorithms. The proposed architecture includes one low frequency normal DNN submodule, and one (or a few) high frequency MscaleDNN submodule(s), which are designed to capture the smooth part and the oscillatory part of the multi-scale solutions, respectively. In addition, a novel trigonometric activation function is incorporated in the SD²NN model. We demonstrate the performance of the SD²NN architecture through several benchmark multi-scale problems in regular or irregular geometric domains. Numerical results show that the SD²NN model is superior to existing models such as MscaleDNN.

Mathematics Subject Classifications: 52B10; 65D18; 68U05; 68U07

Keywords: Multi-scale; DNN; Fourier; Subspace-decomposed; Activation function

1. Introduction

Machine learning algorithms, especially deep neural networks (DNNs), have not only achieved great success in traditional artificial intelligence tasks such as image recognition, natural language processing, and recommendation systems [1, 2], but also attracted more and more attention in the field of scientific computation including the numerical solution of ordinary/partial differential equations, integral-differential equations and dynamical systems [3–8], with the fast development of novel computing devices, as well as the rapidly increasing volume and complexity of data. In this paper, we will introduce a new DNN-based algorithm to solve the following multi-scale equation,

$$\begin{cases} \mathcal{L}u(\mathbf{x}) = f(\mathbf{x}), & \mathbf{x} \in \Omega, \\ \mathcal{B}u(\mathbf{x}) = g(\mathbf{x}), & \mathbf{x} \in \partial\Omega, \end{cases} \quad (1.1)$$

where Ω is a bounded subset of \mathbb{R}^d with piecewise Lipschitz boundary which satisfies the interior cone condition. \mathcal{L} is a linear or non-linear elliptic type differential operator on Ω which contains possibly non-separable multiple scales, and \mathcal{B} is a boundary operator on $\partial\Omega$. We assume that \mathcal{L} is uniformly strongly elliptic such that $\int_{\Omega} v' \mathcal{L}v \geq c\|v\|_{\mathcal{V}}$ for some admissible space \mathcal{V} , with a constant $c > 0$.

*Corresponding author.

Email addresses: lixian9131@163.com, lixa0415@sjtu.edu.cn (Xi-An Li), xuzhiqin@sjtu.edu.cn (Zhi-Qin John Xu), Lzhang2012@sjtu.edu.cn (Lei Zhang)

The multi-scale equation (1.1) has many physical and engineering applications, such as heat conduction in composite materials, reservoir modeling in porous media, convection dominated flows and the Poisson-Boltzmann model for dielectric systems [9–12]. There has been amount of work concerning the design of multi-scale numerical methods to achieve the optimal balance of accuracy and complexity, such as homogenization [13, 14], heterogeneous multi-scale methods (HMM) [15, 16], multi-scale network approximations [17], multi-scale finite element methods (MsFEM)[18], variational multi-scale methods (VMS) [19, 20], flux norm homogenization [21, 22], rough polyharmonic splines (RPS) [23, 24], generalized multi-scale finite element methods (GMsFEM) [25, 26], localized orthogonal decomposition (LOD) [27, 28], etc. A common theme of the multi-scale methods is to construct coarse approximation spaces with optimal error control through the identification of low dimensional structures in the high dimensional multi-scale solution space. The solution space can be decomposed into a direct sum of a coarse space (with “smooth” components) and (possibly a few) fine spaces (with “oscillatory” components), which is a natural extension of the Fourier decomposition. The idea of subspace decomposition has been widely used in numerical analysis and multi-scale modeling [19, 27, 29, 30], furthermore, it has surprisingly deep connections with Bayesian inference, kernel learning and probabilistic numerics [31–34].

Comparing with conventional numerical algorithms, DNN approximation can overcome the curse of dimensionality, therefore it is ideal for high dimensional PDEs. On the other hand, it can be used as a meshless method which is suitable for PDEs in complex domains. Various DNN based algorithms have been proposed in [4, 6, 35, 36] to solve PDEs. Despite the above mentioned progress, the frequency principle (F-Principle) [37–40] shows that general DNN-based algorithms often encounter a “curse of high-frequency” as they are inefficient to learn high-frequency information of multiscale functions. A series of subsequent theoretical investigations further confirm such empirical observation [38, 41–47]. The study of the F-Principle has also been utilized to understand various phenomena emerging in applications of deep learning [48–52]. Inspired by the F-Principle, a series of algorithms are developed to solve multi-scale PDEs and to overcome the high-frequency curse of general DNNs [53–58]. For example, in MscaleDNN, high frequency components are shifted into low frequency ones by radial scaling such that they can be learnt more efficiently. In addition, some smooth and localized activation functions were proposed for MscaleDNN algorithm [56, 57].

In this paper, motivated by the subspace decomposition technique in numerical analysis, and the MscaleDNN framework [56, 57], we propose a subspace-decomposition based DNN (called SD²NN) architecture to solve the multi-scale equation (1.1). The SD²NN framework consists of two parts: one low-frequency or normal DNN submodule and one (or a few) MscaleDNN submodule(s), to capture the low-frequency and high-frequency components of the multi-scale solution, respectively. We enforce the orthogonality between subspaces in the SD²NN architecture to enforce the stability of the decomposition, by adding a penalty term to the loss function. Such a framework enables simultaneous fast learning of both the smooth part and the oscillatory part of multiscale functions/solutions, thus avoids the curse of frequency. We also improve the activation function by adding a relaxation factor and using trigonometric functions [53, 59], which will be elaborated in the later sections.

The paper is organized as follows. In Section 2, we briefly introduce the subspace decomposition based DNN framework to approximate multi-scale functions. In Section 3, we use the SD²NN framework to solve multi-scale problems in the variational formulation, and discuss various options to choose activation functions. Benchmark numerical experiments are carried out in Section 4 to evaluate the performance of SD²NN. We conclude the paper in Section 5.

2. Formulation of the Subspace Decomposition based DNN

2.1. Multi-scale DNN (MscaleDNN)

We briefly review the formulation of MscaleDNN introduced in [56, 57], for convenience of readers. A deep neural network defines a function mapping: $\mathbf{x} \in \mathbb{R}^d \rightarrow y_{\theta}(\mathbf{x}) \in \mathbb{R}$, where d is the dimension of input. In particular, the DNN function is a nested composition of linear functions and nonlinear activation functions,

which is of the form

$$\begin{cases} \mathbf{y}_\theta^{[0]} = \mathbf{x} \\ \mathbf{y}_\theta^{[\ell]} = \sigma \circ (\mathbf{W}^{[\ell]} \mathbf{y}_\theta^{[\ell-1]} + \mathbf{b}^{[\ell]}), \text{ for } \ell = 1, 2, 3, \dots, L \end{cases} \quad (2.1)$$

where $\mathbf{W}^{[\ell]} \in \mathbb{R}^{m_{\ell+1} \times m_\ell}$, $\mathbf{b}^{[\ell]} \in \mathbb{R}^{m_{\ell+1}}$ are the weight matrix and bias vector of the ℓ -th hidden layer, respectively, $m_0 = d$ and m_{L+1} is the dimension of the output, “ \circ ” stands for the elementary-wise operation. $\sigma(\cdot)$ is an element-wise activation function. We also denote the output of DNNs by $\mathbf{y}(\mathbf{x}; \boldsymbol{\theta})$ with $\boldsymbol{\theta}$ standing for the parameter set $(\mathbf{W}^{[1]}, \dots, \mathbf{W}^{[L]}, \mathbf{b}^{[1]}, \dots, \mathbf{b}^{[L]})$.

A normal DNN is usually inadequate to solve multi-scale PDEs as it tends to stagnate on low frequency components. The MscaleDNN architecture was proposed [56, 57] based on the frequency principle to alleviate this problem. It is illustrated in Figure 1 and described in the following: We first divide the neurons in the first hidden-layer into Q parts, and construct the following vector

$$\Lambda = (\overbrace{a_1, \dots, a_1}^{N_1}, \overbrace{a_2, \dots, a_2}^{N_2}, \dots, \overbrace{a_Q, \dots, a_Q}^{N_Q})^T \quad (2.2)$$

where $\{a_q\}_{q=1}^Q$ are positive scale-factors (usually in ascending order), and $\{N_q\}_{q=1}^Q$ are the number of the duplicated q -th scale-factor. The input data \mathbf{x} is scaled by Λ such that $\tilde{\mathbf{x}} = \Lambda \odot (\mathbf{W}^1 \mathbf{x} + \mathbf{b}^1)$, then $\tilde{\mathbf{x}}$ is fed into the subsequent module of MscaleDNN, here and hereinafter \odot stands for the element-wise product.

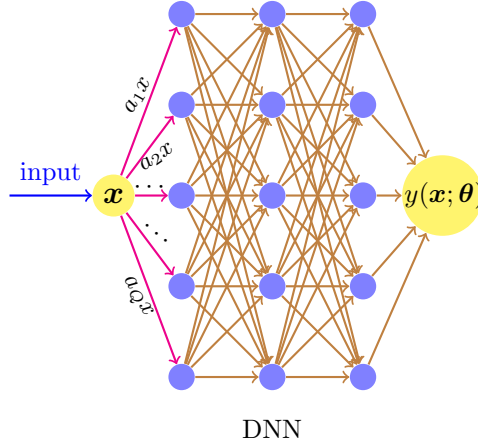


Figure 1: A schematic diagram for MScaleDNN with $N_i = 1, i = 1, \dots, Q$.

From the viewpoint of function approximation, the first layer of the MscaleDNN model can be regarded as a series of basis functions with various scales and the output of MscaleDNN is the (nonlinear) combination of those basis functions [53, 56, 57].

We use the residual neural network (ResNet) [60] to overcome the vanishing gradient phenomenon in backpropagation by introducing skip connections between nonadjacent layers. For example, the ResNet unit with one-step connection produces a filtered version $\mathbf{y}^{[\ell+1]}(\mathbf{x}; \boldsymbol{\theta})$ for the input $\mathbf{y}^{[\ell]}(\mathbf{x}; \boldsymbol{\theta})$ is as follows

$$\mathbf{y}^{[\ell+1]}(\mathbf{x}; \boldsymbol{\theta}) = \mathbf{y}^{[\ell]}(\mathbf{x}; \boldsymbol{\theta}) + \sigma \circ \left(\mathbf{W}^{[\ell+1]} \mathbf{y}^{[\ell]}(\mathbf{x}; \boldsymbol{\theta}) + \mathbf{b}^{[\ell+1]} \right).$$

ResNet can accelerate the training process and improve the performance of DNNs. For scientific computation tasks, it can help improve the capability of DNNs to approximate high-order derivatives and solutions of PDEs [61, 62].

2.2. Subspace decomposition

It is natural to decompose multi-scale solutions into smooth components and oscillatory components. For example, in periodic homogenization with $\mathcal{L} = -\nabla \cdot a(x/\epsilon)\nabla$, the solution u^ϵ of $\mathcal{L}u^\epsilon = f$ can be approximated by $u_0 + \epsilon u_1$, such that u_0 is the solution of the homogenized equation $\mathcal{L}^0 u_0 = f$, where $\mathcal{L}^0 = -\nabla \cdot A\nabla$ with A being the homogenized coefficient. u_0 is much smoother than u^ϵ , and $u_1 = \epsilon \sum_{i=1}^d \chi_i(x/\epsilon) \frac{\partial u_0}{\partial x_i}$ characterizes the oscillations. χ_i is the so-called corrector of the homogenization problem or solution of the cell problem [14, 63], such that

$$\begin{cases} -\nabla_y \cdot a(y)(\nabla_y \xi_i(y) + e_i) = 0, \\ \xi_i \text{ periodic in } Y. \end{cases} \quad (2.3)$$

where $y = x/\epsilon$, and Y is the unit periodic cell.

In many numerical homogenization type multi-scale methods such as VMS, RPS and LOD methods [19, 20, 23, 24, 27, 28, 64], a coarse solution is computed in a low dimensional approximation space V_c with quasi-optimal approximation, stability and localization properties. The bases in V_c contain fine scale information, and they can be pre-computed in localized subdomains in parallel. For some multi-scale problems, numerical homogenization methods can be proved to achieve guaranteed quantitative error estimate with respect to coarse resolutions. Furthermore, multi-scale methods can be considered as two level numerical methods, and can be generalized as multilevel subspace decomposition to construct multigrid type preconditioners for the efficient resolution of fine scale problem, see [30, 65].

3. SD²NN model to multi-scale problems and the options for activation function

3.1. Unified SD²NN architecture to solve multi-scale problems

We introduce subspace-decomposed DNN (called SD²NN) architecture in the following. For simplicity, we employ the deep Ritz method [61] for the solution of multi-scale PDEs (1.1). Other architectures such as PINN [66], deep Galerkin [35] etc. can be adapted.

Continuous variational formulation. The solution of (1.1) can be obtained by minimizing the following Dirichlet energy

$$\mathcal{J}(v) = \frac{1}{2} \int_{\Omega} v' \mathcal{L} v d\mathbf{x} - \int_{\Omega} f v d\mathbf{x}, \quad (3.1)$$

where $v = v(\mathbf{x}) \in \mathcal{V}$ is a trial function, where \mathcal{V} is the admissible function space for v . We are looking for the solution

$$u = \arg \min_{v \in \mathcal{V}} \mathcal{J}(v).$$

Suppose that the solution u has the following coarse/fine decomposition, $u = u_c + u_f$, in which u_c contains the coarse shape and u_f contains the fine details of the multi-scale solution u , respectively. Formally, (3.1) can be rewritten as

$$\mathcal{J}(v_c, v_f) = \frac{1}{2} \int_{\Omega} (v_c + v_f)' \mathcal{L}(v_c + v_f) d\mathbf{x} - \int_{\Omega} f(v_c + v_f) d\mathbf{x}. \quad (3.2)$$

To ensure the well-posedness of the variational problem with respect to v_c and v_f , we need to define the respective subspaces \mathcal{V}_c and \mathcal{V}_f , in where v_c and v_f "live", which will be specified in the particular examples. The coarse part v_c can be represented by a low-frequency or a normal DNN $y_1(\cdot, \boldsymbol{\theta}_1)$, and the fine-part (or high-frequency part) u_f can be represented by a multi-scale DNN $y_2(\cdot, \boldsymbol{\theta}_2)$. Here, $\boldsymbol{\theta}_1 \in \Theta_1$ and $\boldsymbol{\theta}_2 \in \Theta_2$ denote the parameters of the underlying DNNs. In this case, we have

$$\begin{aligned} \mathcal{V}_c &= \left\{ y_1(\mathbf{x}; \boldsymbol{\theta}_1) \mid y_1(\mathbf{x}; \boldsymbol{\theta}_1) = g, \mathbf{x} \in \partial\Omega; \boldsymbol{\theta}_1 \in \Theta_1 \right\}, \\ \mathcal{V}_f &= \left\{ y_2(\mathbf{x}; \boldsymbol{\theta}_2) \mid y_2(\mathbf{x}; \boldsymbol{\theta}_2) = 0, \mathbf{x} \in \partial\Omega; \boldsymbol{\theta}_2 \in \Theta_2 \right\}. \end{aligned} \quad (3.3)$$

Remark. Here we present the SD^2NN model as a two level model, and it can be easily generalized to a multilevel model by adding more $MscaleDNN$ submodules with appropriate frequency factors. We will illustrate this point through Example 2 in the numerics section.

We further introduce a hyper-parameter $\alpha > 0$ to control the contribution of fine-part, i.e., $y(\mathbf{x}; \boldsymbol{\theta}_1, \boldsymbol{\theta}_2) = y_1(\mathbf{x}; \boldsymbol{\theta}_1) + \alpha y_2(\mathbf{x}; \boldsymbol{\theta}_2)$. Let

$$\begin{aligned} \mathcal{J}_\alpha \left(y_1(\mathbf{x}; \boldsymbol{\theta}_1), y_2(\mathbf{x}; \boldsymbol{\theta}_2) \right) &= \frac{1}{2} \int_{\Omega} \left(y_1(\mathbf{x}; \boldsymbol{\theta}_1) + \alpha y_2(\mathbf{x}; \boldsymbol{\theta}_2) \right)' \mathcal{L} \left(y_1(\mathbf{x}; \boldsymbol{\theta}_1) + \alpha y_2(\mathbf{x}; \boldsymbol{\theta}_2) \right) d\mathbf{x} \\ &\quad - \int_{\Omega} f \left(y_1(\mathbf{x}; \boldsymbol{\theta}_1) + \alpha y_2(\mathbf{x}; \boldsymbol{\theta}_2) \right) d\mathbf{x}, \end{aligned} \quad (3.4)$$

we then obtain the following variational problem

$$u_c, u_f = \arg \min_{y_1(\mathbf{x}; \boldsymbol{\theta}_1) \in \mathcal{V}_c, y_2(\mathbf{x}; \boldsymbol{\theta}_2) \in \mathcal{V}_f} \mathcal{J}_\alpha \left(y_1(\mathbf{x}; \boldsymbol{\theta}_1), y_2(\mathbf{x}; \boldsymbol{\theta}_2) \right)$$

Discrete Variational Formulation. The integral in (3.4) can be discretized by Monte Carlo method [67], namely, we define

$$L_{\mathcal{J}_\alpha}(S_I; \boldsymbol{\theta}_1, \boldsymbol{\theta}_2) = \frac{1}{n_{in}} \sum_{i=1}^{n_{in}} \left[\frac{1}{2} \left(y_1(\mathbf{x}_I^i; \boldsymbol{\theta}_1) + \alpha y_2(\mathbf{x}_I^i; \boldsymbol{\theta}_2) \right)' \mathcal{L} \left(y_1(\mathbf{x}_I^i; \boldsymbol{\theta}_1) + \alpha y_2(\mathbf{x}_I^i; \boldsymbol{\theta}_2) \right) - f \left(y_1(\mathbf{x}_I^i; \boldsymbol{\theta}_1) + \alpha y_2(\mathbf{x}_I^i; \boldsymbol{\theta}_2) \right) \right],$$

here and hereinafter S_I stands for the sampling points with uniform distribution in Ω , and

$$\boldsymbol{\theta}_1^*, \boldsymbol{\theta}_2^* = \arg \min_{\boldsymbol{\theta}_1 \in \Theta_1, \boldsymbol{\theta}_2 \in \Theta_2} L_{\mathcal{J}_\alpha}(S_I; \boldsymbol{\theta}_1, \boldsymbol{\theta}_2),$$

such that $u_c = y_1(\mathbf{x}; \boldsymbol{\theta}_1^*)$, $u_f = \alpha y_2(\mathbf{x}; \boldsymbol{\theta}_2^*)$.

Orthogonality constraints. In order to separate the coarse-part and fine-part of solution, we add the L^2 orthogonality constraint $\int_{\Omega} y_1(\mathbf{x}; \boldsymbol{\theta}) \cdot \alpha y_2(\mathbf{x}; \boldsymbol{\theta}) d\mathbf{x} = 0$ as a penalty term to the loss function, namely, let

$$L_{orth}(S_I; \boldsymbol{\theta}_1, \boldsymbol{\theta}_2) = \left| \frac{1}{n_{in}} \sum_{i=1}^{n_{in}} y_1(\mathbf{x}_I^i; \boldsymbol{\theta}_1) \cdot \alpha y_2(\mathbf{x}_I^i; \boldsymbol{\theta}_2) \right|^2, \mathbf{x}_I^i \in S_I. \quad (3.5)$$

Boundary condition. Boundary conditions are important constraints for numerical solution of PDEs. According to the definition of coarse and fine spaces (3.3), we have the following penalties for the coarse part $y_1(\mathbf{x}; \boldsymbol{\theta}_1)$ and the fine-part $y_2(\mathbf{x}; \boldsymbol{\theta}_2)$,

$$L_{bdc}(S_B; \boldsymbol{\theta}_1) = \frac{1}{n_{bd}} \sum_{j=1}^{n_{bd}} \left[\mathcal{B}y_1(\mathbf{x}_B^j; \boldsymbol{\theta}_1) - g(\mathbf{x}_B^j) \right]^2 \quad \text{for } \mathbf{x}_B^j \in S_B, \quad (3.6)$$

and

$$L_{bdf}(S_B; \boldsymbol{\theta}_2) = \frac{1}{n_{bd}} \sum_{j=1}^{n_{bd}} \left[\mathcal{B}\alpha y_2(\mathbf{x}_B^j; \boldsymbol{\theta}_2) - 0 \right]^2 \quad \text{for } \mathbf{x}_B^j \in S_B. \quad (3.7)$$

For comparison, we also introduce the penalty for the "unified" boundary condition of $y(\mathbf{x}; \boldsymbol{\theta}_1, \boldsymbol{\theta}_2) = y_1(\mathbf{x}; \boldsymbol{\theta}_1) + \alpha y_2(\mathbf{x}; \boldsymbol{\theta}_2)$, i.e.,

$$L_{bdu}(S_B; \boldsymbol{\theta}_1) = \frac{1}{n_{bd}} \sum_{j=1}^{n_{bd}} \left[\mathcal{B}y(\mathbf{x}_B^j; \boldsymbol{\theta}_1, \boldsymbol{\theta}_2) - g(\mathbf{x}_B^j) \right]^2 \quad \text{for } \mathbf{x}_B^j \in S_B, \quad (3.8)$$

with S_B standing for the collection of sampling points with uniform distribution on $\partial\Omega$.

We conclude with the following loss function:

$$L_\alpha(S_I, S_B; \boldsymbol{\theta}_1, \boldsymbol{\theta}_2) = \underbrace{L_{\mathcal{J}_\alpha}(S_I; \boldsymbol{\theta}_1, \boldsymbol{\theta}_2)}_{loss_in} + \underbrace{\gamma \left(L_{bdc}(S_B; \boldsymbol{\theta}_1) + L_{bdf}(S_B; \boldsymbol{\theta}_2) \right)}_{loss_bd} + \underbrace{\beta L_{orth}(S_I; \boldsymbol{\theta}_1, \boldsymbol{\theta}_2)}_{loss_orth} \quad (3.9)$$

with $S_I = \{\mathbf{x}_I^i\}_{i=1}^{n_{it}}$ and $S_B = \{\mathbf{x}_B^j\}_{j=1}^{n_{bd}}$ being the sets of uniformly distributed sample points on Ω and $\partial\Omega$, respectively. The first term $loss_in$ minimizes the residual of the PDE, the second term $loss_bd$ enforces the given boundary condition, and the third term $loss_dot$ imposes the orthogonality constraint. In addition, we introduce two penalty parameter γ and β to control the contribution of $loss_bd$ and $loss_orth$ for loss function, in which γ is increasing gradually during the training process [68] and β is a fixed constant.

Our goal is to find two sets of parameter $\boldsymbol{\theta}_1, \boldsymbol{\theta}_2$ which minimize the loss function $L_\alpha(S_I, S_B; \boldsymbol{\theta}_1, \boldsymbol{\theta}_2)$, i.e.,

$$\boldsymbol{\theta}_1^*, \boldsymbol{\theta}_2^* = \arg \min L_\alpha(S_I, S_B; \boldsymbol{\theta}_1, \boldsymbol{\theta}_2) \implies u_c(\mathbf{x}), u_f(\mathbf{x}) = y_1(\mathbf{x}; \boldsymbol{\theta}_1^*), \alpha y_2(\mathbf{x}; \boldsymbol{\theta}_2^*).$$

If $L_\alpha(S_I, S_B; \boldsymbol{\theta}_1, \boldsymbol{\theta}_2)$ is small enough, then $y(\mathbf{x}; \boldsymbol{\theta}_1, \boldsymbol{\theta}_2)$ will be very close to the solution of (1.1). The parameter $\boldsymbol{\theta}_1$ and $\boldsymbol{\theta}_2$ can be computed by stochastic gradient descent method with a pre-defined learning rate schedule. We use the Xavier initialization for the weights and biases [69, 70]. In other word, the weights and biases are sampled from normal distribution $\mathcal{D} = \mathcal{N}\left(0, \frac{2}{m_{in} + m_{out}}\right)$, where m_{in} and m_{out} are the input and output dimensions of the corresponding layer, respectively.

3.2. Options for activation function

The choice of activation functions is crucial for the performance of DNN based algorithms. Two localized activation functions, namely, $sReLU(\mathbf{x}) = \text{ReLU}(\mathbf{x}) * \text{ReLU}(1 - \mathbf{x})$ and $s2ReLU(\mathbf{x}) = \sin(2\pi\mathbf{x}) * \text{ReLU}(\mathbf{x}) * \text{ReLU}(1 - \mathbf{x})$ were proposed for MscaleDNN in [56, 57]. Heuristic analysis and numerical results show that the latter one is smoother and more robust. However, these two activation functions are supported in range $[0, 1]$, therefore the output will become zero if the input is outside the interval $[0, 1]$. This will affect the performance of MscaleDNN in the training process.

In this work, we propose the following *soften Fourier mapping (SFM)* activation function inspired by the trigonometric activation function proposed in [53, 54, 59], namely,

$$\sigma(\mathbf{z}) = s \times \begin{bmatrix} \cos(\mathbf{z}) \\ \sin(\mathbf{z}) \end{bmatrix},$$

where the *relaxation* parameter $s \in (0, 1]$ is used to control the range of output. Empirically, we find that $s = 0.5$ is a good choice, see Fig. 2. With the SFM activation function, the MscaleDNN can be regard as a pipeline of Fourier-like transform. The first hidden layer of the MscaleDNN architecture mimic the Fourier expansion, and the remaining structure learns the approximate Fourier coefficients, which are often relatively less oscillate with respect to the input. In this sense, the learning can be effectively accelerated.

The above mentioned activation functions are illustrated in Fig. 3.

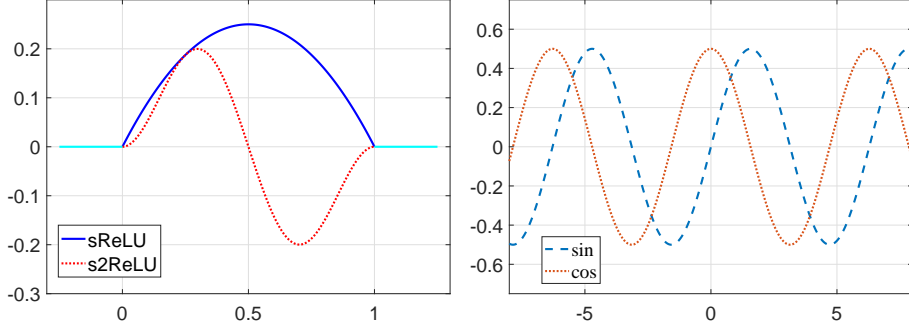


Figure 2: sReLU and s2ReLU functions (left), SFM functions with $s = 0.5$ (right).

We conclude the section with the schematic of the SD²NN architecture in Figure 3. The output of SD²NN is obtained by a linear layer with no activation function.

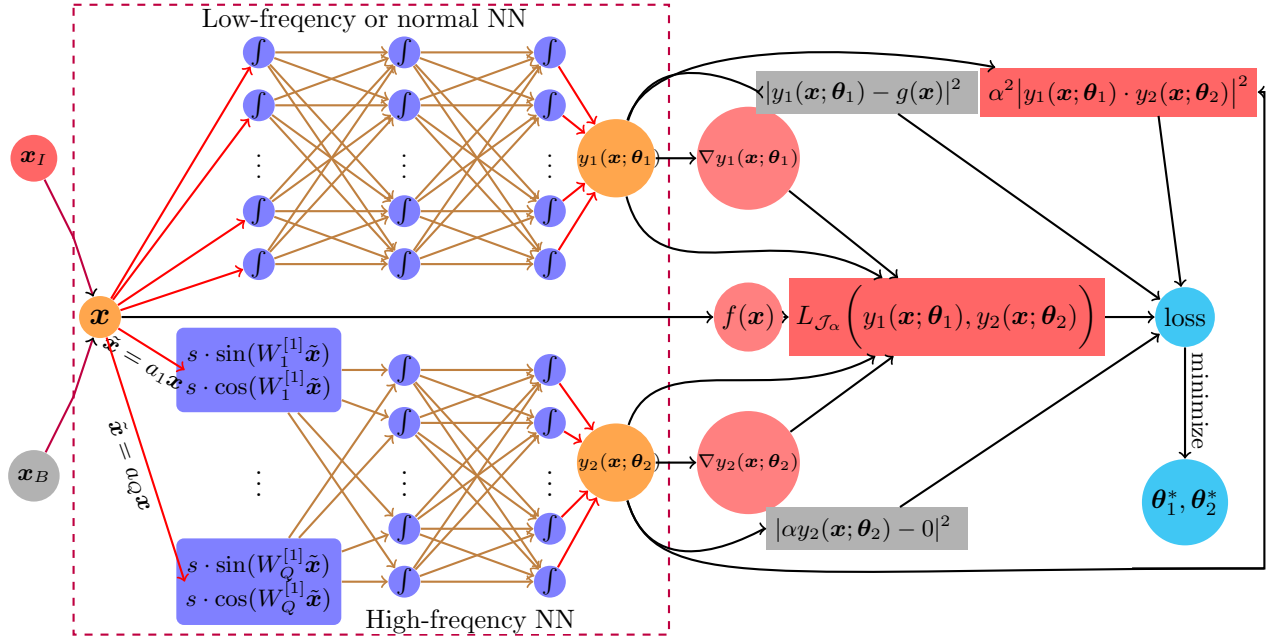


Figure 3: Schematic of SD²NN for solving multi-scale problems

4. Numerical experiments

In this section, we test the performance of SD²NN method for multi-scale problems with highly oscillatory coefficients and Poisson-Boltzmann equation in perforated domains. We demonstrate that the SD²NN method can efficiently and simultaneously solve the coarse part and the fine part of the multi-scale solution. We also investigated the effects of different activation functions (for example, SFM and s2ReLU). We show that SD²NN has better performance compared with existing methods such as MscaleDNN in [53, 57].

4.1. Model and training setup

4.1.1. Model setup

The details of all the models in the numerical experiments are elaborated in the following.

- *SD²NN1*: We use a normal fully-connected DNN as the coarse submodule and a high-frequency MscaleDNN as the fine submodule. The first layer of the fine submodule has scaling factors $\Lambda = (21, 22, 23, \dots, 120)$ with $Q = 100$, as in (2.2). The activation function for each hidden layer in the normal DNN is chosen as $\tanh(x)$, the activation functions for the first hidden layer and the subsequent layers of MscaleDNN are chosen as SFM with $s = 0.5$ and s2ReLU, respectively.
- *SD²NN2*: We use a low-frequency MscaleDNN as the coarse submodule and a high-frequency MscaleDNN as the fine submodule. The first layers of coarse submodule and fine submodule have scaling factors $\Lambda_c = (0.5, 1, 1.5, 2, \dots, 19.5, 20)$ with $Q = 40$, and $\Lambda_f = (21, 22, 23, \dots, 120)$ with $Q = 100$, respectively. The activation function for their first hidden layers are all chosen as SFM with $s = 1.0$ and $s = 0.5$ (denoted as SFM(1.0) and SFM(0.5)), but the activation functions for their subsequent layers are chosen as $\tanh(x)$ and s2ReLU, respectively.
- *SD²NN3*: The activation functions and scaling factors are same as *SD²NN2*. But we take away the orthogonality penalty term (3.9) from the loss function, and the boundary condition is the unified one in (3.8).
- *Mscale*: A MscaleDNN model [57] with s2ReLU activation function for all layers. The neurons of the first layer are divided into $Q = 120$ groups with scaling factors $\Lambda = (1, 2, 3, \dots, 119, 120)$ in (2.2).
- *WWP*: A MscaleDNN model [53] with hybrid activation function including SFM with $s = 1.0$ (denoted as SFM(1.0)) and $\tanh(x)$. The scaling factors of the first layer are divided as four subgroups. Each subgroup has 30 samples from Gaussian distribution $\mathcal{N}(0; \tau_i^2)$ with $\tau_1 = 1$, $\tau_2 = 20$, $\tau_3 = 50$ and $\tau_4 = 100$. This model is proposed by Wang, Wang, and Perdikaris in [53], and we denote it as *WWP*.

Table 1: Comparisons for the above models

Model	Submodules	Activation	Scale factor	Boundary	Orthogonality
SD ² NN1	Normal	tanh	—	individual boundary (3.6) and (3.7)	Yes
	MscaleDNN	SFM(0.5)+s2ReLU	(21, 22, 23, \dots , 120)		
SD ² NN2	MscaleDNN	SFM(1.0)+tanh	(0.5, 1, 1.5, 2, \dots , 19.5, 20)	individual boundary (3.6) and (3.7)	Yes
	MscaleDNN	SFM(0.5)+s2ReLU	(21, 22, 23, \dots , 120)		
SD ² NN3	MscaleDNN	SFM(1.0)+tanh	(0.5, 1, 1.5, 2, \dots , 19.5, 20)	unified boundary (3.8)	No
	MscaleDNN	SFM(0.5)+s2ReLU	(21, 22, 23, \dots , 120)		
Mscale	—	s2ReLU	(1, 2, 3, \dots , 119, 120)	unified boundary (3.8)	—
WWP	—	SFM(1.0)+tanh	$\Lambda = [\Lambda_1; \Lambda_2; \Lambda_3; \Lambda_4]$ with $\Lambda_i \sim \mathcal{N}(0, \tau_i)$, $\tau_1 = 1$, $\tau_2 = 20, \tau_3 = 50, \tau_4 = 100$	unified boundary (3.8)	—

4.1.2. Training setup

We use the relative square error to evaluate the accuracy of different models:

$$REL = \sum_{i=1}^{N'} \frac{|\tilde{u}(\mathbf{x}^i) - u^*(\mathbf{x}^i)|^2}{|u^*(\mathbf{x}^i)|^2}$$

where $\tilde{u}(\mathbf{x}^i)$ and $u^*(\mathbf{x}^i)$ are the approximate DNN solution and the exact solution, respectively, $\{\mathbf{x}^i\}_{i=1}^{N'}$ are testing points, and N' is the number of testing points.

In our numerical experiments, all training and testing data are sampled uniformly in Ω (or $\partial\Omega$), and all networks are trained by Adam optimizer. The initial learning rate is set as 2×10^{-4} with a decay rate 5×10^{-5} for each training epoch. For visualization of the training process, we test our model every 1000 epochs in the training process. The penalty parameter β for the orthogonality constraint (3.5) is set as 20,

γ for the boundary constraint (3.6) and (3.7) is set as

$$\gamma = \begin{cases} \gamma_0, & \text{if } i_{\text{epoch}} < 0.1T_{\text{max}} \\ 10\gamma_0, & \text{if } 0.1T_{\text{max}} \leq i_{\text{epoch}} < 0.2T_{\text{max}} \\ 50\gamma_0, & \text{if } 0.2T_{\text{max}} \leq i_{\text{epoch}} < 0.25T_{\text{max}} \\ 100\gamma_0, & \text{if } 0.25T_{\text{max}} \leq i_{\text{epoch}} < 0.5T_{\text{max}} \\ 200\gamma_0, & \text{if } 0.5T_{\text{max}} \leq i_{\text{epoch}} < 0.75T_{\text{max}} \\ 500\gamma_0, & \text{otherwise} \end{cases} \quad (4.1)$$

where $\gamma_0 = 100$ in all our tests and T_{max} represents the total epoch number. We implement our code in TensorFlow (version 1.14.0) on a work station (256-GB RAM, single NVIDIA GeForce GTX 2080Ti 12-GB).

4.2. Numerical examples and results

In this section, we test the SD²NN models for multi-scale diffusion and Poisson-Boltzmann equations.

Example 1 (1D multi-scale elliptic problem). We use this problem to benchmark our models. Let us consider the following multi-scale elliptic equation in domain $\Omega = [a, b]^d$

$$\begin{cases} -\operatorname{div}\left(A(\mathbf{x})|\nabla u(\mathbf{x})|^{p-2}\nabla u(\mathbf{x})\right) = f(\mathbf{x}), & \mathbf{x} \in \Omega, \\ u(\mathbf{x}) = g(\mathbf{x}), & \mathbf{x} \in \partial\Omega. \end{cases} \quad (4.2)$$

which has the following Dirichlet energy

$$\mathcal{J}(v) = \frac{1}{p} \int_{\Omega} A|\nabla v|^p d\mathbf{x} - \int_{\Omega} fvd\mathbf{x}. \quad (4.3)$$

Linear Case:

We first consider the linear case $p = 2$ with $\Omega = [0, 1]$ and boundary condition $u(0) = u(1) = 0$,

$$A(x) = \left(2 + \cos\left(2\pi\frac{x}{\epsilon}\right)\right)^{-1} \quad (4.4)$$

with a small parameter $\epsilon > 0$ such that $\epsilon^{-1} \in \mathbb{N}^+$, the unique solution is given by

$$u(x) = x - x^2 + \epsilon \left(\frac{1}{4\pi} \sin\left(2\pi\frac{x}{\epsilon}\right) - \frac{1}{2\pi} x \sin\left(2\pi\frac{x}{\epsilon}\right) - \frac{\epsilon}{4\pi^2} \cos\left(2\pi\frac{x}{\epsilon}\right) + \frac{\epsilon}{4\pi^2} \right). \quad (4.5)$$

for $f(x) = 1$.

We use MscaleDNNs and SD²NNs with aforementioned setups to solve (4.2) when $\epsilon = 0.1$ and $\epsilon = 0.01$, respectively. For comparison, a normal DNN model with *tanh* activation function (denoted by DNN) is also employed to solve this multi-scale problem. In SD²NN models, the balance parameter α for fine-part is set as 0.01. The number of parameters are comparable for different models (see Table 4 in Appendix A). At each training step, we randomly sample 3000 interior points and 500 boundary points to evaluate the loss function. All models are trained for 60000 epochs. In the testing step, we uniformly sample 1000 points in $[0, 1]$. We show the testing results for $\epsilon = 0.1$ and $\epsilon = 0.01$ in Figures 4 and 5, respectively.

Table 2: The relative error of different models for Example 1 when $\alpha = 0.01$.

	DNN	Mscale	WWP	SD ² NN1	SD ² NN2	SD ² NN3
$\epsilon = 0.1$	2.40e-2	3.42e-6	3.84e-6	1.36e-5	6.22e-7	7.81e-7
$\epsilon = 0.01$	2.05e-2	6.95e-3	1.94e-2	2.80e-4	7.69e-7	3.30e-5

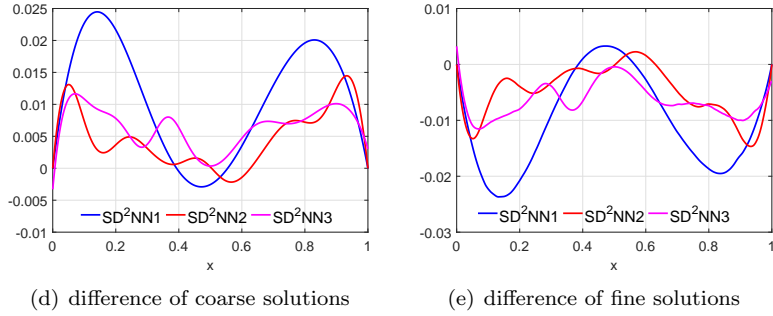
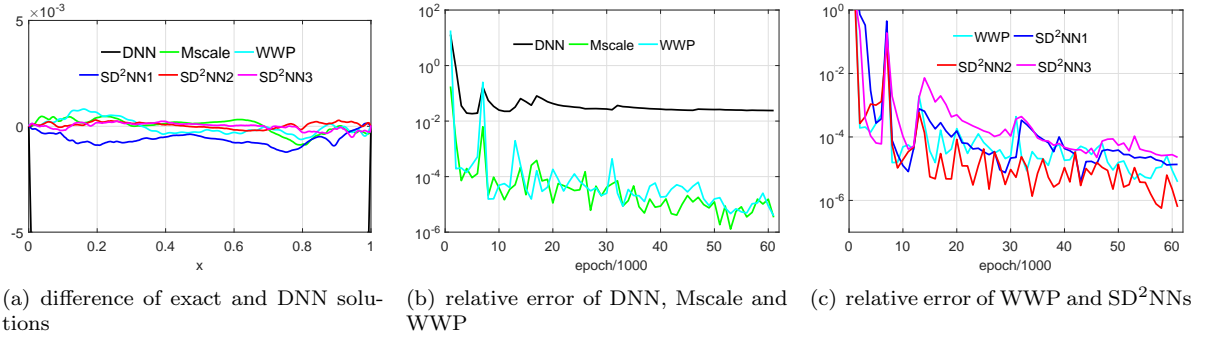


Figure 4: Testing results with $\epsilon = 0.1$ for Example 1.

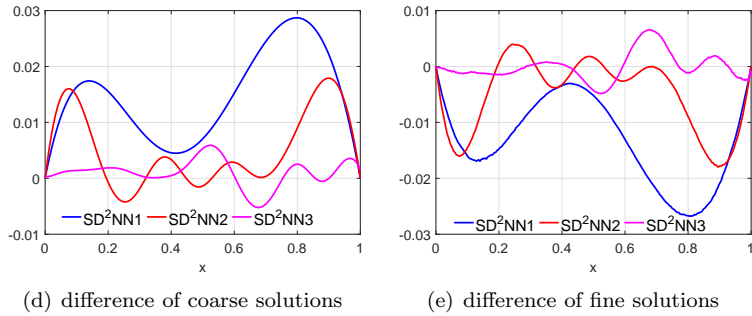
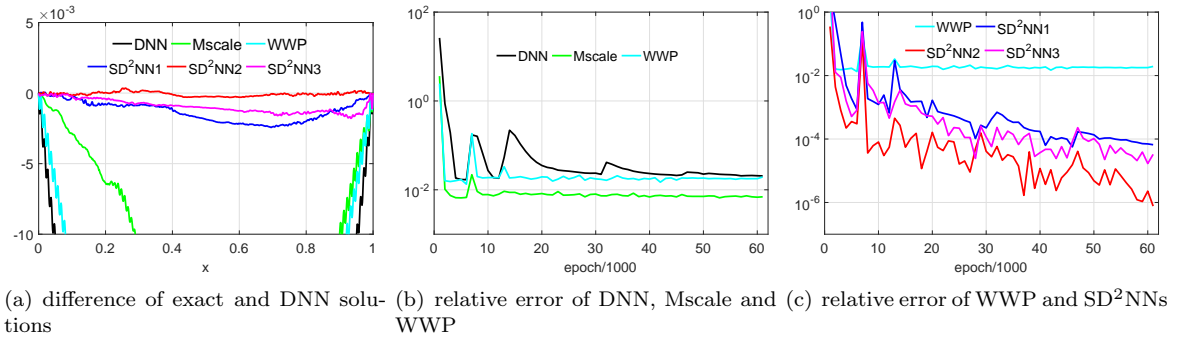


Figure 5: Testing results when $\epsilon = 0.01$ for Example 1.

From Figures 4(a) and 5(a), we observe that all three SD^2NN models capture the exact solutions with $\epsilon = 0.1$ and $\epsilon = 0.01$ pretty well. By comparison, the performances of Mscale and WWP are okay for the case $\epsilon = 0.1$, but deteriorate for the more oscillatory case $\epsilon = 0.01$. The normal DNN model fails in both

cases. Figures 4(b), 4(c), 5(b) and 5(c) and the relative errors in Table 2 further demonstrate that SD²NN2 is the best method. For the $\epsilon = 0.01$ case, the error of SD²NN2 is smaller than other methods by at least two orders of magnitude.

We choose the coarse part of the exact solution $u(x)$ as $u^c(x) := x - x^2$, and the fine part $u^f(x)$ as the remainder. Though it is not unique to choose the fine (and coarse) parts, they are “equivalent” if the difference is smooth. We draw the differences of coarse solutions of SD²NN1, SD²NN2 and SD²NN3 with $u^c(x)$ in Figures 4(d) and 5(d), and the differences of fine solutions with $u^f(x)$ in Figures 4(e) and 5(e). The differences are smooth, which shows that SD²NN models can capture the correct coarse and fine components of the solution.

Influence of hyper-parameter α : we study the influence of α for SD²NN model. In the test, we set $\alpha = 0.05$, $\epsilon = 0.01$, keep all other parameters fixed, then train all models for 60000 epochs. Based on the results in Figure 6, we observe that SD²NN2 is more stable and accurate compared to all other models.

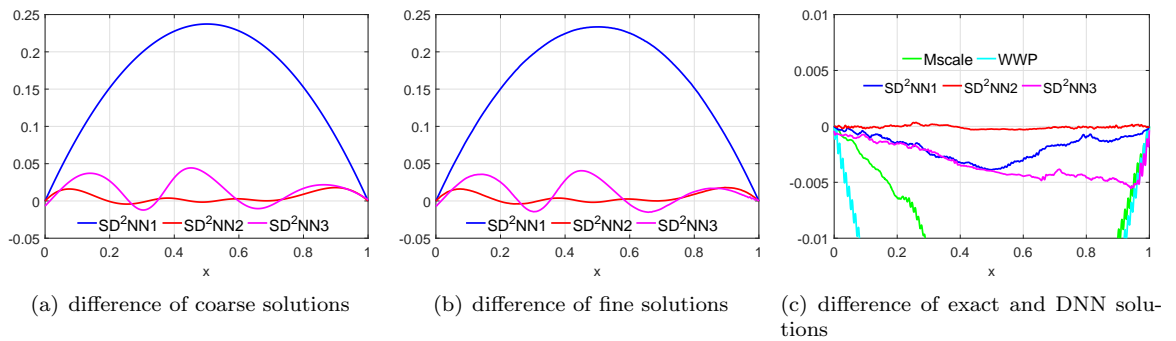


Figure 6: Testing results when $\epsilon = 0.01$ for Example 1.

Influence of relaxation-parameter s : we study the influence of relaxation-parameter s for activation function SFM in SD²NN model, especially for SD²NN2. Here, we list the setup of SD²NN2 in Table 1, as well as two alternative setups:

- SD²NN2: SFM(1.0)+tanh for coarse submodule and SFM(0.5)+S2ReLU for fine submodule;
- SD²NN2(a): SFM(0.5)+tanh for coarse submodule and SFM(0.5)+S2ReLU for fine submodule;
- SD²NN2(b): SFM(1.0)+tanh for coarse submodule and SFM(1.0)+S2ReLU for fine submodule.

we set $\alpha = 0.05$, $\epsilon = 0.01$, and train both models for 60000 epochs. From the results in Figure 7, it seems for the fine submodule of SD²NN2, a relaxed parameter $s = 0.5$ offers better performance.

Nonlinear Case:

We further consider the nonlinear case with $p = 8$ for (4.2) with $\Omega = [0, 1]$ and $A(x) = (2 + \cos(2\pi \frac{x}{\epsilon}))^{-1}$. By choosing appropriate $f(x)$, the (unique) solution is given by

$$u(x) = x - x^2 + \epsilon \left(\frac{1}{4\pi} \sin\left(2\pi \frac{x}{\epsilon}\right) - \frac{1}{2\pi} x \sin\left(2\pi \frac{x}{\epsilon}\right) - \frac{\epsilon}{4\pi^2} \cos\left(2\pi \frac{x}{\epsilon}\right) + \frac{\epsilon}{4\pi^2} \right). \quad (4.6)$$

with $u_\epsilon(0) = u_\epsilon(1) = 0$.

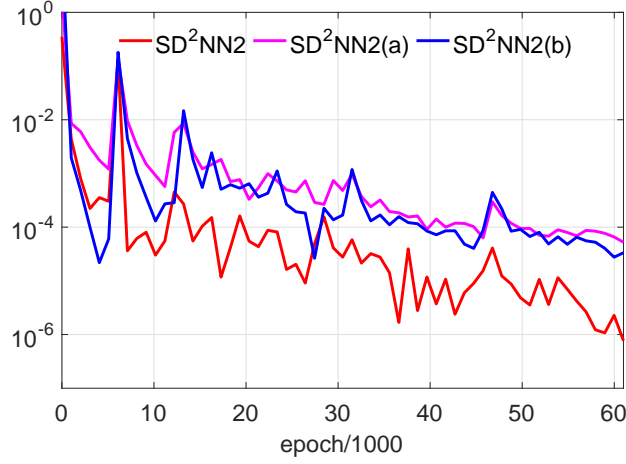


Figure 7: Relative error for SD^2NN2 when $\epsilon = 0.01$ for Example 1.

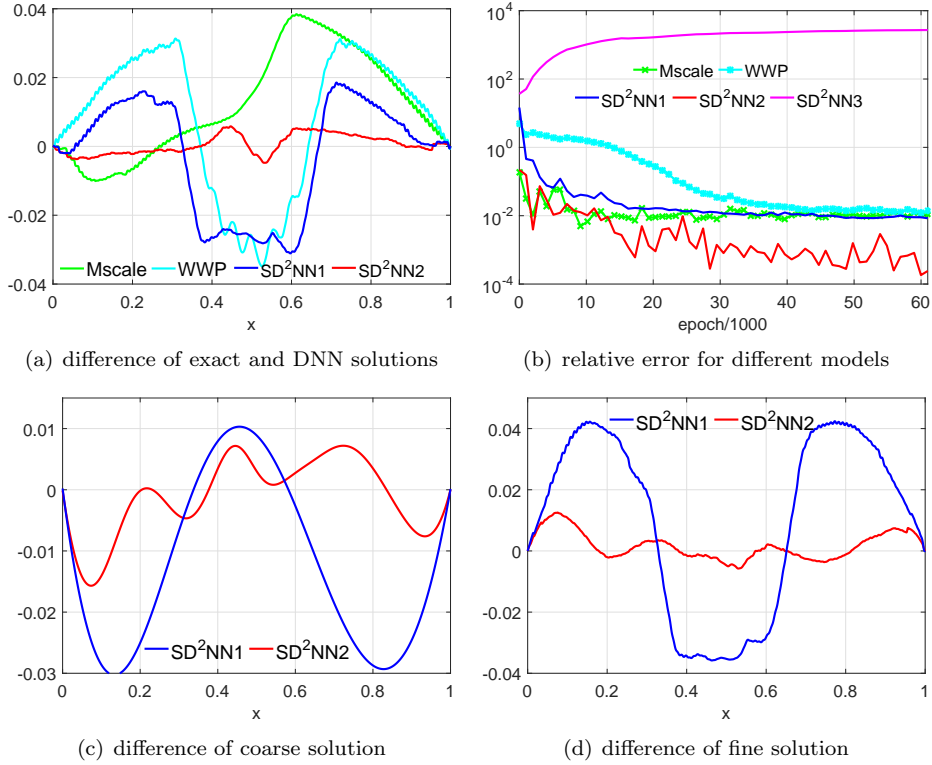


Figure 8: Testing results for $\epsilon = 0.01$ and $p = 8$.

We employ Mscale, WWP and SD^2NN2 models to solve (4.2). Based on the results in Figure 8, the SD^2NN2 model still outperform Mscale, WWP, SD^2NN1 and SD^2NN3 (fails to converge) for nonlinear multi-scale problem. In addition, the differences of coarse and fine solutions in Figures 8(c) and 8(d) show that the submodules of SD^2NN2 also can well capture the coarse and fine parts of the multi-scale solution.

Example 2 (Three-scale problem). We solve the problem (4.2) with the following three-scale coefficient

$$A(x) = \left(2 + \cos\left(2\pi\frac{x}{\epsilon_1}\right)\right) \left(2 + \cos\left(2\pi\frac{x}{\epsilon_2}\right)\right) \quad (4.7)$$

with two small parameter $1 \gg \epsilon_1 \gg \epsilon_2 > 0$, also for $p = 2$ and $\Omega = [0, 1]$. We impose the exact solution

$$u(x) = x - x^2 + \frac{\epsilon_1}{4\pi} \sin\left(2\pi\frac{x}{\epsilon_1}\right) + \frac{\epsilon_2}{4\pi} \sin\left(2\pi\frac{x}{\epsilon_2}\right). \quad (4.8)$$

with $u(0) = u(1) = 0$, such that $f(x)$ can be obtained by direct computation.

We employ the aforementioned Mscale, WWP, SD²NN1, SD²NN2 and SD²NN3 to solve (4.2) with (4.7) with $\epsilon_1 = 0.1$ and $\epsilon_2 = 0.01$. We use 2 MscaleDNN submodules in the SD²NN models, and the balance parameters $\alpha_1 = 0.1$ and $\alpha_2 = 0.01$ for the mesoscale submodule and the fine submodule, respectively. Table 5 in Appendix A shows that the number of parameters for different models are comparable. All models are trained for 60000 epochs. For each training step, we randomly sample 3000 interior points and 500 boundary points as the training data, and uniformly sample 1000 points in $[0, 1]$ as the testing data.

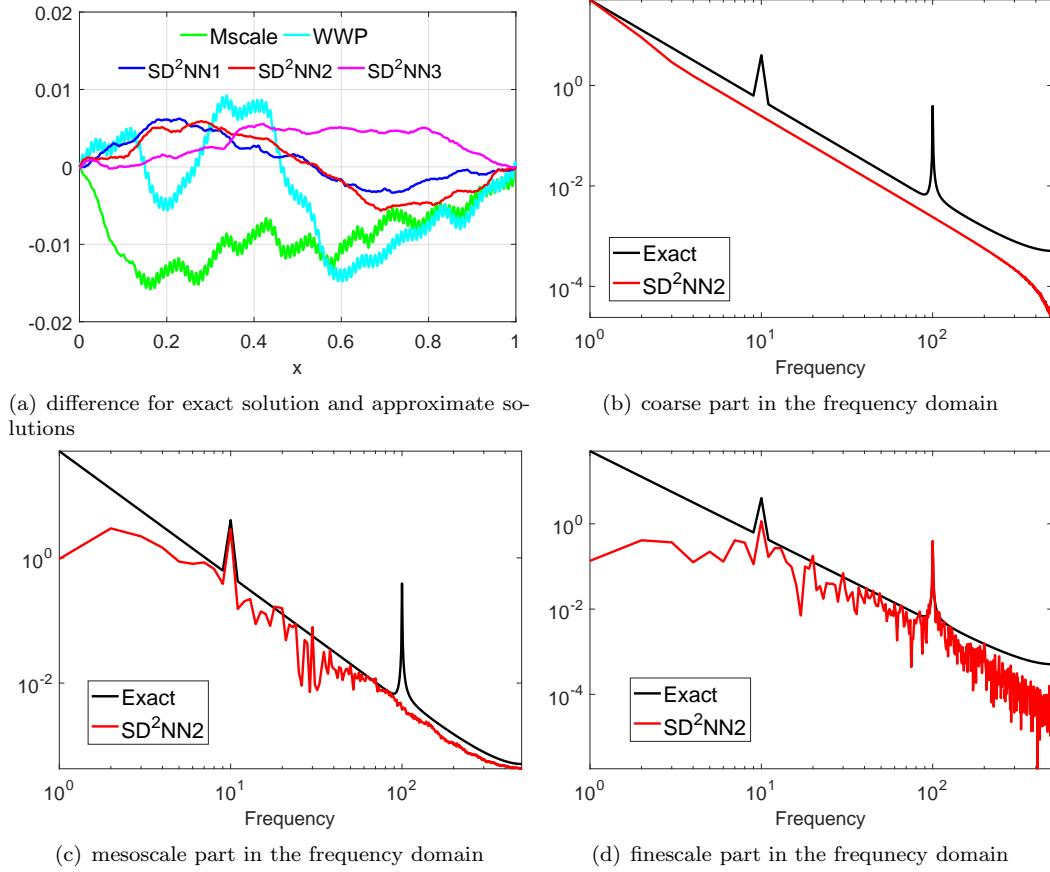


Figure 9: Numerical results for Example 2

Table 3: The relative error of different models for Example 2

Mscale	WWP	SD ² NN1	SD ² NN2	SD ² NN3
2.70e-3	1.53e-3	1.25e-3	6.75e-5	1.55e-4

In Figure 9(a), we draw the difference of the approximate solution and the numerical solution, together with the relative errors from Table 3, it shows that SD²NN2 is the best method. In Figures 9(b) – 9(d) we compare the coarse, mesoscale, fine scale parts of the SD²NN2 solution with the exact solution, in the frequency domain. We demonstrate that three submodules of the SD²NN2 model can correctly capture the corresponding components of the solution as they are supposed to be.

From now on, we will only consider the Mscale, WWP and SD²NN2 models in the following examples.

Example 3. We consider the following two-dimensional problem (4.2) for $p = 2$ and $\Omega = [-1, 1] \times [-1, 1]$. In this example, we set $f = 1$ and the multi-scale coefficient

$$A(x_1, x_2) = \prod_{i=1}^6 \left(1 + 0.5 \cos(2^i \pi(x_1 + x_2)) \right) \left(1 + 0.5 \sin(2^i \pi(x_2 - 3x_1)) \right).$$

from [71–73]. The reference solution $u(x_1, x_2)$ can be computed by the finite element method on a square grid of mesh-size $h = 1/129$.

We compute the solution of (4.2) by Mscale, WWP and SD²NN2, respectively. In the SD²NN2 model, the balance parameter α for fine-submodule is 0.05. The network size and parameter number for different models are comparable and listed in Table 6 in Appendix A. All models are trained for 100000 epochs. At each training step, we sample 3000 interior points and 500 boundary points. The testing points are taken from the finite element grid with $h = 1/129$.

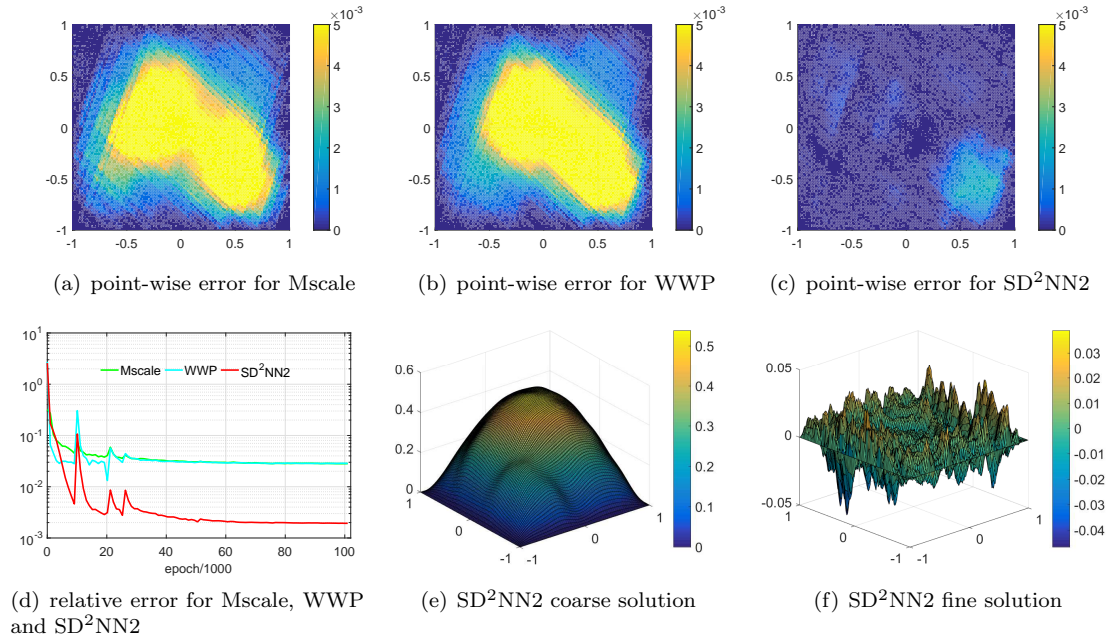


Figure 10: Testing results for Example 3

The numerical results in Figures 10(a) – 10(d) show that the SD²NN2 is still the method of choice in terms of both the point-wise error and the mean square error, and it is much better than Mscale and WWP models. In addition, the results in Figures 10(e) and 10(f) show that the submodules of SD²NN2 successfully separate the coarse and fine parts of the solution.

Example 4. We now consider the following Poisson-Boltzmann equation with Dirichlet boundary condition,

$$\begin{cases} -\operatorname{div}(A(\mathbf{x})\nabla u(\mathbf{x})) + \kappa(\mathbf{x})u(\mathbf{x}) = f(\mathbf{x}), & \mathbf{x} \in \Omega \subset \mathbb{R}^d, \\ u(\mathbf{x}) = g(\mathbf{x}), & \mathbf{x} \in \partial\Omega \end{cases} \quad (4.9)$$

where $A_\epsilon(\mathbf{x})$ is the dielectric constant and $\kappa(\mathbf{x})$ the inverse Debye-Huckel length of an ionic solvent. It is natural to introduce the energy

$$\mathcal{J}(v) = \frac{1}{2} \int_{\Omega} \left(A|\nabla v|^2 + \kappa v^2 \right) d\mathbf{x} - \int_{\Omega} f v d\mathbf{x}. \quad (4.10)$$

and the corresponding variational formulation.

We solve the elliptic equation (4.9) in the cube $\Omega = [0, 1]^3$ with 8 big holes (blue) and 27 smaller holes (red), see Figure 11(a). We take $\kappa(x_1, x_2, x_3) = \pi^2$,

$$A(x_1, x_2, x_3) = 0.5 \left(2 + \cos(10\pi x_1) \cos(20\pi x_2) \cos(30\pi x_3) \right), \quad (4.11)$$

and impose an exact solution

$$u(x_1, x_2, x_3) = \sin(\pi x_1) \sin(\pi x_2) \sin(\pi x_3) + 0.05 \sin(10\pi x_1) \sin(20\pi x_2) \sin(30\pi x_3). \quad (4.12)$$

The exact solution prescribes the corresponding boundary condition and $f(x)$ in (4.9).

In this example, the network sizes and the number of parameter for Mscale, WWP and SD²NN2 are listed in Table 7 in Appendix A, their parameters are comparable. In addition, the balance parameter $\alpha = 0.05$ for the fine-part of SD²NN2. All models are trained for 100000 epochs. At each training step, the training data set including 6000 interior points and 1000 boundary points randomly sampled from Ω and $\partial\Omega$. The testing dataset is 1600 random samples in Ω . Testing results are plotted in Fig.11.

From the results in 11(b) – 11(d), the SD²NN2 model still keeps its good performance for the Poisson-Boltzmann equation in 3D perforated domain.

5. Conclusion

Deep learning algorithms have demonstrated great potential in scientific computing tasks. However, the efficient solution of multi-scale problems remains to be a big challenge for DNN based numerical methods. In this paper, we combine subspace decomposition ideas from traditional numerical analysis and multi-scale deep neural network, and propose the *SD²NN* method for multi-scale PDEs. This new architecture consists of one low-frequency or normal DNN submodule and one (or several) high-frequency MscaleDNN submodule(s). In addition, we incorporate the trigonometric *SFM* activation function for the SD²NN model. Computational results show that this new method is feasible and efficient for multi-scale problems in 1d, 2d and 3d, and in both regular or perforated domains. In the future, we plan to apply this method to multi-scale PDEs with nonlinearity and/or randomness, as well as operator learning for multi-scale PDEs.

Acknowledgements

X.A.L and L.Z are partially supported by the National Natural Science Foundation of China (NSFC 11871339, 11861131004). Z.X. is supported by the National Key R&D Program of China Grant No. 2019YFA0709503, the Shanghai Sailing Program, the Natural Science Foundation of Shanghai Grant No. 20ZR1429000, the National Natural Science Foundation of China Grant No. 62002221, Shanghai Municipal of Science and Technology Project Grant No. 20JC1419500, Shanghai Municipal of Science and Technology Major Project NO. 2021SHZDZX0102, and the HPC of School of Mathematical Sciences and the Student Innovation Center at Shanghai Jiao Tong University. Thanks to Xin-Liang Liu for his some codes and helpful suggestions.

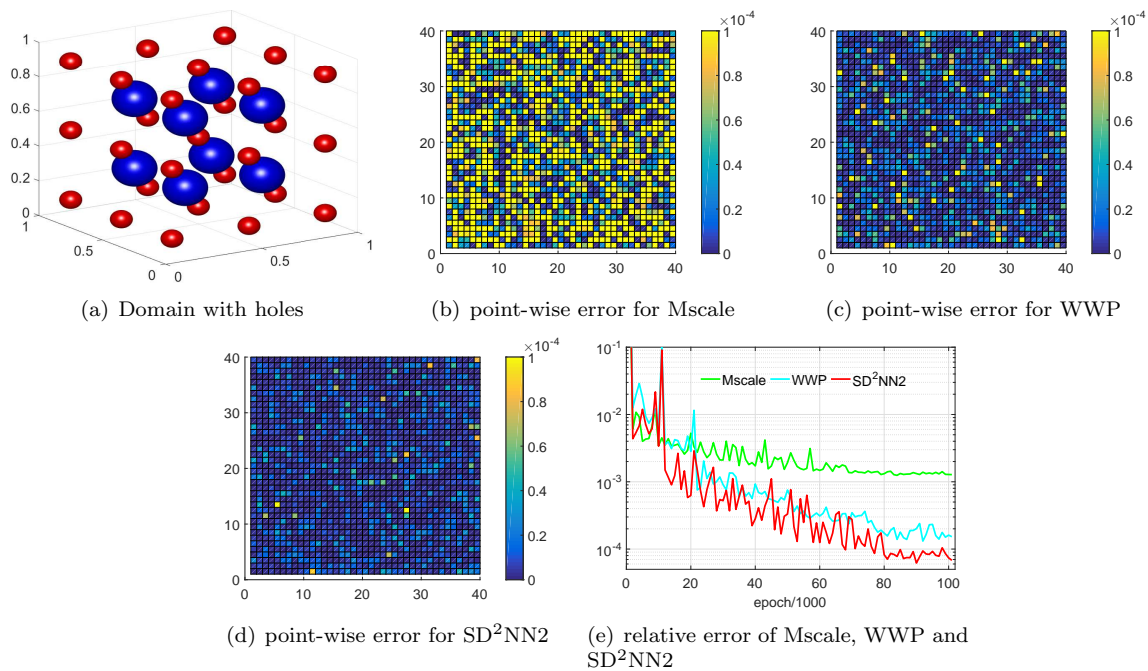


Figure 11: Testing results for Example 4.

References

- [1] Y. LeCun, Y. Bengio, G. Hinton, Deep learning, *Nature* 521 (2015) 436–444.
- [2] I. Goodfellow, Y. Bengio, A. Courville, *Deep Learning*, MIT press, Cambridge, 2016.
- [3] W. E, A Proposal on Machine Learning via Dynamical Systems, *Communications in Mathematics and Statistics* 5 (2017) 1–11.
- [4] W. E, J. Han, A. Jentzen, Deep learning-based numerical methods for high-dimensional parabolic partial differential equations and backward stochastic differential equations, *Communications in Mathematics and Statistics* 5 (2017) 349–380.
- [5] J. Han, L. Zhang, R. Car, et al., Deep Potential: A General Representation of a Many-Body Potential Energy Surface, *Communications in Computational Physics* 23 (2018).
- [6] M. Raissi, P. Perdikaris, G. E. Karniadakis, Physics-informed neural networks: A deep learning framework for solving forward and inverse problems involving nonlinear partial differential equations, *Journal of Computational Physics* 378 (2019) 686–707.
- [7] E. Weinan, *Machine learning and computational mathematics*, arXiv preprint arXiv:2009.14596 (2020).
- [8] E. Shi, C. Xu, A comparative investigation of neural networks in solving differential equations, *Journal of Algorithms & Computational Technology* 15 (2021) 1–15.
- [9] H. Owhadi, Anomalous slow diffusion from perpetual homogenization, *Ann. Probab.* 31 (2003) 1935–1969.
- [10] N. Homeyer, H. Gohlke, Free Energy Calculations by the Molecular Mechanics Poisson-Boltzmann Surface Area Method., *Molecular Informatics* 31 (2012) 114–122.
- [11] G. J. M. Hagelaar, L. C. Pitchford, Solving the Boltzmann equation to obtain electron transport coefficients and rate coefficients for fluid models, *Plasma Sources Science and Technology* 14 (2005) 722–733.
- [12] A. Cohen, W. Dahmen, G. Welper, Adaptivity and variational stabilization for convection-diffusion equations, *Mathematical Modelling and Numerical Analysis* 46 (2012) 1247–1273.
- [13] G. Papanicolau, A. Bensoussan, J.-L. Lions, *Asymptotic analysis for periodic structures*, Elsevier, 1978.
- [14] V. Jikov, S. M. Kozlov, O. A. Oleinik, *Homogenization of differential operators and integral functionals*, Springer Science & Business Media, 2012.
- [15] W. E, B. Engquist, Heterogeneous multiscale methods, *Comm. Math. Sci.* 1 (2003) 87–132.
- [16] P. Ming, P. Zhang, et al., Analysis of the heterogeneous multiscale method for elliptic homogenization problems, *Journal of the American Mathematical Society* 18 (2005) 121–156.
- [17] L. Berlyand, A. G. Kolpakov, A. Novikov, *Introduction to the network approximation method for materials modeling*, volume 148, Cambridge University Press, 2013.
- [18] T. Y. Hou, X.-H. Wu, A multiscale finite element method for elliptic problems in composite materials and porous media, *Journal of Computational Physics* 134 (1997) 169–189.

- [19] T. J. R. Hughes, G. Feijoo, L. Mazzei, J. Quincy, The variational multiscale method—a paradigm for computational mechanics, *Comput. Methods Appl. Mech. Engrg.* 166 (1998) 3–24.
- [20] Y. Bazilevs, V. Calo, J. Cottrell, T. Hughes, A. Reali, G. Scovazzi, Variational multiscale residual-based turbulence modeling for large eddy simulation of incompressible flows, *Computer Methods in Applied Mechanics and Engineering* 197 (2007) 173–201.
- [21] L. Berlyand, H. Owhadi, Flux norm approach to finite dimensional homogenization approximations with non-separated scales and high contrast, *Archive for rational mechanics and analysis* 198 (2010) 677–721.
- [22] H. Owhadi, L. Zhang, Homogenization of parabolic equations with a continuum of space and time scales, *SIAM Journal on Numerical Analysis* 46 (2008) 1–36.
- [23] H. Owhadi, L. Zhang, L. Berlyand, Polyharmonic homogenization, rough polyharmonic splines and sparse super-localization, *ESIAM* 48 (2014) 517–552.
- [24] X. Liu, L. Zhang, S. Zhu, Generalized rough polyharmonic splines for multiscale pdes with rough coefficients, *Numerical Mathematics: Theory, Methods and Applications* 14 (2021) 862–892.
- [25] Y. Efendiev, J. Galvis, T. Hou, Generalized multiscale finite element methods, *Journal of Computational Physics* 251 (2013) 116–135.
- [26] E. T. Chung, Y. Efendiev, W. T. Leung, An adaptive generalized multiscale discontinuous galerkin method for high-contrast flow problems, *Multiscale Modeling & Simulation* 16 (2018) 1227–1257.
- [27] A. Målqvist, D. Peterseim, Localization of elliptic multiscale problems, *Math. Comp.* 83 (2014) 2583–2603.
- [28] P. Henning, A. Målqvist, D. Peterseim, A localized orthogonal decomposition method for semi-linear elliptic problems, *ESAIM Math. Model. Numer. Anal.* 48 (2014) 1331–1349.
- [29] J. Xu, Iterative methods by space decomposition and subspace correction, *SIAM review* 34 (1992) 581–613.
- [30] H. Xie, L. Zhang, H. Owhadi, Fast eigenpairs computation with operator adapted wavelets and hierarchical subspace correction, *SIAM Journal on Numerical Analysis* 57 (2019) 2519–2550.
- [31] H. Owhadi, Bayesian numerical homogenization, *Multiscale Model. Simul.* 13 (2015) 812–828.
- [32] H. Owhadi, Multigrid with rough coefficients and Multiresolution operator decomposition from Hierarchical Information Games, *SIAM Rev.* 59 (2017) 99–149.
- [33] H. Owhadi, C. Scovel, G. R. Yoo, Kernel mode decomposition and programmable/interpretable regression networks, *arXiv preprint arXiv:1907.08592* (2019).
- [34] H. Owhadi, G. R. Yoo, Kernel flows: From learning kernels from data into the abyss, *Journal of Computational Physics* 389 (2019) 22–47.
- [35] J. Sirignano, K. Spiliopoulos, DGM: A deep learning algorithm for solving partial differential equations, *Journal of Computational Physics* 375 (2018) 1339–1364.
- [36] Y. Zang, G. Bao, X. Ye, H. Zhou, Weak adversarial networks for high-dimensional partial differential equations, *Journal of Computational Physics* 411 (2020) 109409.
- [37] Z.-Q. J. Xu, Y. Zhang, Y. Xiao, Training behavior of deep neural network in frequency domain, *International Conference on Neural Information Processing* (2019) 264–274.
- [38] Z.-Q. J. Xu, Y. Zhang, T. Luo, Y. Xiao, Z. Ma, Frequency Principle: Fourier Analysis Sheds Light on Deep Neural Networks, *Communications in Computational Physics* 28 (2020) 1746–1767.
- [39] N. Rahaman, D. Arpit, A. Baratin, F. Draxler, M. Lin, F. A. Hamprecht, Y. Bengio, A. Courville, On the spectral bias of deep neural networks, *International Conference on Machine Learning* (2019).
- [40] Y. Zhang, T. Luo, Z. Ma, Z.-Q. J. Xu, A linear frequency principle model to understand the absence of overfitting in neural networks, *Chinese Physics Letters* 38 (2021) 038701.
- [41] T. Luo, Z. Ma, Z.-Q. J. Xu, Y. Zhang, Theory of the Frequency Principle for General Deep Neural Networks, *arXiv preprint arXiv:1906.09235* (2019).
- [42] B. Ronen, D. Jacobs, Y. Kasten, S. Kritchman, The convergence rate of neural networks for learned functions of different frequencies, in: *Advances in Neural Information Processing Systems*, volume 32, 2019, pp. 4761–4771.
- [43] W. E, C. Ma, L. Wu, Machine learning from a continuous viewpoint, *arXiv preprint arXiv:1912.12777* (2019).
- [44] Y. Cao, Z. Fang, Y. Wu, D.-X. Zhou, Q. Gu, Towards understanding the spectral bias of deep learning, *arXiv preprint arXiv:1912.01198* (2019).
- [45] G. Yang, H. Salman, A fine-grained spectral perspective on neural networks, *arXiv preprint arXiv:1907.10599* (2019).
- [46] B. Bordelon, A. Canatar, C. Pehlevan, Spectrum dependent learning curves in kernel regression and wide neural networks, in: *Proceedings of the 37th International Conference on Machine Learning, ICML 2020, 13-18 July 2020, Virtual Event*, volume 119 of *Proceedings of Machine Learning Research*, PMLR, 2020, pp. 1024–1034.
- [47] T. Luo, Z. Ma, Z.-Q. J. Xu, Y. Zhang, On the exact computation of linear frequency principle dynamics and its generalization, *arXiv preprint arXiv:2010.08153* (2020).
- [48] C. Ma, L. Wu, W. E, The slow deterioration of the generalization error of the random feature model, in: *Mathematical and Scientific Machine Learning*, PMLR, 2020, pp. 373–389.
- [49] R. Sharma, A. Ross, D-netpad: An explainable and interpretable iris presentation attack detector, in: *2020 IEEE International Joint Conference on Biometrics (IJCB)*, IEEE, 2020, pp. 1–10.
- [50] H. Zhu, Y. Qiao, G. Xu, L. Deng, Y. Yu-Feng, Dspnet: A lightweight dilated convolution neural networks for spectral deconvolution with self-paced learning, *IEEE Transactions on Industrial Informatics* (2019).
- [51] P. Chakrabarty, S. Maji, The spectral bias of the deep image prior, *arXiv preprint arXiv:1912.08905* (2019).
- [52] Z.-Q. J. Xu, H. Zhou, Deep frequency principle towards understanding why deeper learning is faster, in: *Proceedings of the AAAI Conference on Artificial Intelligence*, volume 35, 2021.
- [53] S. Wang, H. Wang, P. Perdikaris, On the eigenvector bias of fourier feature networks: From regression to solving multi-

- scale pdes with physics-informed neural networks, *Computer Methods in Applied Mechanics and Engineering* 384 (2021) 113938.
- [54] W. Cai, X. Li, L. Liu, A phase shift deep neural network for high frequency approximation and wave problems, *SIAM Journal on Scientific Computing* 42 (2020) A3285–A3312.
- [55] A. D. Jagtap, K. Kawaguchi, G. E. Karniadakis, Adaptive activation functions accelerate convergence in deep and physics-informed neural networks, *Journal of Computational Physics* 404 (2020) 109136.
- [56] Z. Liu, W. Cai, Z.-Q. J. Xu, Multi-scale deep neural network (mscalednn) for solving poisson-boltzmann equation in complex domains, *Communications in Computational Physics* 28 (2020) 1970–2001.
- [57] X.-A. Li, Z.-Q. J. Xu, L. Zhang, A multi-scale dnn algorithm for nonlinear elliptic equations with multiple scales, *Communications in Computational Physics* 28 (2020) 1886–1906.
- [58] B. Wang, W. Zhang, W. Cai, Multi-scale deep neural network (mscalednn) methods for oscillatory stokes flows in complex domains, *Communications in Computational Physics* 28 (2020) 2139–2157.
- [59] M. Tancik, P. P. Srinivasan, B. Mildenhall, S. Fridovich-Keil, N. Raghavan, U. Singhal, R. Ramamoorthi, J. T. Barron, R. Ng, Fourier features let networks learn high frequency functions in low dimensional domains, *arXiv preprint arXiv:2006.10739* (2020).
- [60] K. He, X. Zhang, S. Ren, J. Sun, Deep residual learning for image recognition, in: *2016 IEEE Conference on Computer Vision and Pattern Recognition (CVPR)*, 2016, pp. 770–778.
- [61] W. E, B. Yu, The Deep Ritz Method: A Deep Learning-Based Numerical Algorithm for Solving Variational Problems, *Communications in Mathematics and Statistics* 6 (2018) 1–12.
- [62] Z. Zou, H. Zhang, Y. Guan, J. Zhang, Deep residual neural networks resolve quartet molecular phylogenies., *Molecular Biology and Evolution* 37 (2020) 1495–1507.
- [63] J. L. Lions, A. Bensoussan, G. Papanicolaou, *Asymptotic analysis for periodic structures*, volume 5, North Holland, Amsterdam, 1978.
- [64] T. J. R. Hughes, G. R. Feijóo, L. Mazzei, J.-B. Quinicy, The variational multiscale method—a paradigm for computational mechanics, *Computer Methods in Applied Mechanics and Engineering* 166 (1998) 3–24.
- [65] H. Owhadi, Multigrid with rough coefficients and multiresolution operator decomposition from hierarchical information games, *Siam Review* 59 (2017) 99–149.
- [66] M. Raissi, P. Perdikaris, G. E. Karniadakis, Inferring solutions of differential equations using noisy multi-fidelity data, *Journal of Computational Physics* 335 (2017) 736–746.
- [67] C. P. Robert, G. Casella, *Monte Carlo Statistical Methods*, 1999.
- [68] A. Quarteroni, R. Sacco, F. Saleri, *Numerical Mathematics*, Numerical Mathematics, 2007.
- [69] X. Glorot, Y. Bengio, Understanding the difficulty of training deep feedforward neural networks, in: *Proceedings of the Thirteenth International Conference on Artificial Intelligence and Statistics*, 2010, pp. 249–256.
- [70] G. M. Rotskoff, E. Vanden-Eijnden, Parameters as interacting particles: long time convergence and asymptotic error scaling of neural networks, in: *32nd Conference on Neural Information Processing Systems, NeurIPS 2018*, 2018, pp. 7146–7155.
- [71] H. Owhadi, L. Zhang, Homogenization of Parabolic Equations with a Continuum of Space and Time Scales, *SIAM Journal on Numerical Analysis* 46 (2007) 1–36.
- [72] H. Owhadi, L. Zhang, Numerical homogenization of the acoustic wave equations with a continuum of scales, *Computer Methods in Applied Mechanics and Engineering* 198 (2008) 397–406.
- [73] H. Owhadi, L. Zhang, L. Berlyand, Polyharmonic homogenization, rough polyharmonic splines and sparse super-localization, *Mathematical Modelling and Numerical Analysis* 48 (2014) 517–552.

Appendix

A.

Table 4: Network sizes and number of parameters for models in Example 1

	Network Size	Number of Parameters
DNN	(250, 100, 80, 80, 60)	44510
Mscale	(250, 100, 80, 80, 60)	44510
WWP	(125, 100, 80, 80, 60)	44385
SD ² NN1	coarse:(100, 80, 60, 60, 40) fine:(125, 60, 60, 60, 50)	44440
SD ² NN2	coarse:(50, 80, 60, 60, 40) fine:(100, 60, 60, 50, 40)	44315
SD ² NN3	coarse:(50, 80, 60, 60, 40) fine:(100, 60, 60, 50, 40)	44315

Table 5: Network sizes and number of parameters for models in Example 2

	Network Size	Para.	Scaling factors
Mscale	(350, 300, 200, 200, 100)	225450	—
WWP	(175, 300, 200, 200, 100)	225275	—
SD ² NN1	coarse:(100, 80, 60, 60, 40) mesoscale:(125, 80, 60, 60, 40) fine:(225, 200, 150, 150, 100)	207730	(30, 31, 32, \dots , 69, 70) (251, 252, 253, \dots , 360)
SD ² NN2	coarse:(50, 80, 60, 60, 40) mesoscale:(125, 80, 60, 60, 40) fine:(225, 200, 150, 150, 100)	207680	(0.5, 1, 1.5, \dots , 24.5, 25) (30, 31, 32, \dots , 69, 70) (251, 252, 253, \dots , 360)
SD ² NN3	coarse:(50, 80, 60, 60, 40) mesoscale:(125, 80, 60, 60, 40) fine:(225, 200, 150, 150, 100)	207680	(0.5, 1, 1.5, \dots , 24.5, 25) (30, 31, 32, \dots , 69, 70) (251, 252, 253, \dots , 360)

Table 6: Network sizes and parameter of models for Example 3

	Network Size	Para.
Mscale	(250, 200, 200, 100, 100, 80)	128330
WWP	(125, 200, 200, 100, 100, 80)	128205
SD ² NN2	coarse:(50, 100, 80, 80, 80, 60) fine:(120, 150, 150, 100, 100, 80)	127410

Table 7: Network sizes and parameter of different models for Example 4

	Network Size	Para.
Mscale	(500, 400, 400, 200, 200, 150)	510650
WWP	(250, 400, 400, 200, 200, 150)	510400
SD ² NN2	coarse:(70, 200, 200, 150, 150, 150) fine:(250, 300, 290, 200, 200, 150)	508870